EUROPEAN ORGANIZATION FOR NUCLEAR RESEARCH (CERN)

CERN-EP-2022-010
2022/04/28

CMS-HIG-20-018

Search for light Higgs bosons from supersymmetric cascade decays in pp collisions at $\sqrt{s} = 13\,\text{TeV}$

The CMS Collaboration

Abstract

A search is reported for pairs of light Higgs bosons (H_1) produced in supersymmetric cascade decays in final states with small missing transverse momentum. A data set of LHC pp collisions collected with the CMS detector at $\sqrt{s} = 13\,\text{TeV}$ and corresponding to an integrated luminosity of $138\,\text{fb}^{-1}$ is used. The search targets events where both H_1 bosons decay into $b\bar{b}$ pairs that are reconstructed as large-radius jets using substructure techniques. No evidence is found for an excess of events beyond the background expectations of the standard model (SM). Results from the search are interpreted in the next-to-minimal supersymmetric extension of the SM, where a "singlino" of small mass leads to squark and gluino cascade decays that can predominantly end in a highly Lorentz-boosted singlet-like H_1 and a singlino-like neutralino of small transverse momentum. Upper limits are set on the product of the squark or gluino pair production cross section and the square of the $b\bar{b}$ branching fraction of the H_1 in a benchmark model containing almost mass-degenerate gluinos and light-flavour squarks. Under the assumption of an SM-like $H_1 \to b\bar{b}$ branching fraction, H_1 bosons with masses in the range 40–120 GeV arising from the decays of squarks or gluinos with a mass of 1200 to 2500 GeV are excluded at 95% confidence level.

Submitted to the European Physical Journal C

1 Introduction

This paper presents a search for pairs of light Higgs bosons (H_1) produced in supersymmetric (SUSY) [1–8] cascade decays in final states with small missing transverse momentum (p_T^{miss}). Such events can arise from the pair production of squarks ($\tilde{q}$) and gluinos ($\tilde{g}$) in the next-to-minimal supersymmetric extension of the standard model (SM) [9] when the lightest SUSY particle (LSP) is a singlino-like neutralino ($\tilde{\chi}_S^0$) of small mass [10]. The $\tilde{\chi}_S^0$ mass eigenstate is dominated by the singlino component and has only small couplings to other SUSY particles, suppressing direct squark or gluino decays to the $\tilde{\chi}_S^0$. Squarks and gluinos decay via the next-to-LSP $\tilde{\chi}_2^0$ into a $\tilde{\chi}_S^0$ and a Higgs, Z, or W boson [10, 11]. The case of a singlet-like *CP*-even H_1, shown in Fig. 1, is the focus of this search. When the $\tilde{\chi}_S^0$ has a far smaller mass than the H_1 and the phase space for the decay $\tilde{\chi}_2^0 \to H_1 + \tilde{\chi}_S^0$ is small, the H_1 carries much larger momentum than the $\tilde{\chi}_S^0$. In such p_T^{miss}-suppressed scenarios, the key signature for the pair production of squarks and gluinos is a pair of Lorentz-boosted H_1 bosons.

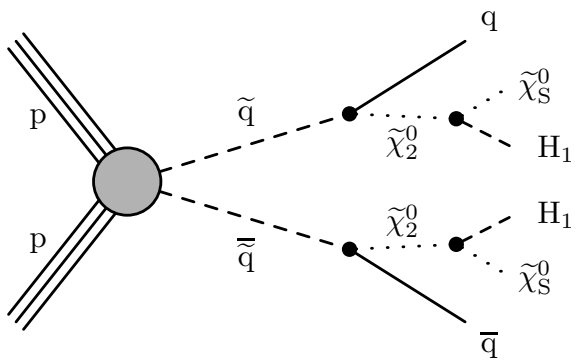

Figure 1: Diagram of squark pair production and subsequent cascade decay in the benchmark signal model. The particle $\tilde{\chi}_2^0$ is the next-to-LSP, $\tilde{\chi}_S^0$ is the singlino-like LSP, and H_1 is the *CP*-even singlet-like Higgs boson.

This search targets events with two highly boosted H_1 bosons that decay into $b\bar{b}$ pairs that are reconstructed as large-radius jets using substructure techniques. This is the first search at the LHC to focus on this type of event, where particles invisible to the detector have only small transverse momentum (p_T) and therefore the events are not selected by searches requiring significant p_T^{miss} [10, 12]. Previous searches by the ATLAS and CMS experiments with similar final states have considered events with two boosted SM Higgs bosons and large values of p_T^{miss} [13, 14], or two SM Higgs bosons in resolved final states where each of the four b quarks is reconstructed as a separate jet, with either small [15] or large [14–17] values of p_T^{miss}. This search uses data from pp collisions collected by the CMS detector at $\sqrt{s} = 13\,\text{TeV}$ during 2016–2018, corresponding to an integrated luminosity of $138\,\text{fb}^{-1}$ [18–20].

2 Benchmark signal model

A benchmark signal model is established following the work of Ellwanger and Teixeira [10, 11]. The eight light-flavour squarks are assumed mass-degenerate at the mass m_{SUSY}, and the gluino mass is set at 1% larger. The small gluino-squark mass gap means that the kinematics of the final-state particles are very similar in the $\tilde{q}\tilde{q}$, $\tilde{q}\tilde{g}$, and $\tilde{g}\tilde{g}$ production modes, as little momentum is transferred to the quark in the $\tilde{g} \to \tilde{q} + q$ decay. All SUSY particles other than gluinos and those shown in Fig. 1 are assumed decoupled.

This search targets squarks and gluinos with $m_{\text{SUSY}} > 1200\,\text{GeV}$. Less massive squarks and gluinos can be probed by $p_{\text{T}}^{\text{miss}}$-based searches, owing to their larger pair-production cross sections [12]. Smaller m_{SUSY} values can also lead to smaller p_{T} of the H_1 than is necessary for the $\text{b}\bar{\text{b}}$ pair to be merged in a single jet. The cross sections (σ) for the signal probed in this search, calculated at next-to-leading order (NLO) accuracy in the strong coupling constant (α_{S}) including approximate next-to-NLO (NNLO) corrections and next-to-next-to-leading logarithmic (NNLL) soft gluon corrections [21–29], are shown in Table 1.

Table 1: Inclusive pair-production cross sections calculated at approximately NNLO and NNLL in α_{S} [21–29] for squark mass m_{SUSY} and gluino mass 1% larger. The quoted uncertainty is obtained from variations in the choice of scales, parton distribution functions, and α_{S}.

m_{SUSY} [GeV]	$\sigma(\text{pp} \to \tilde{\text{q}}\tilde{\text{q}}, \tilde{\text{q}}\tilde{\text{g}}, \tilde{\text{g}}\tilde{\text{g}})$ [fb]	Uncertainty
1200	580	8%
1600	69	9%
2000	10	11%
2200	4.1	13%
2400	1.6	14%
2600	0.67	16%
2800	0.27	18%

The values considered of the H_1 mass (m_{H_1}) and the corresponding $\text{H}_1 \to \text{b}\bar{\text{b}}$ branching fractions ($\mathcal{B}$) are shown in Table 2. Only events where both H_1 bosons decay into $\text{b}\bar{\text{b}}$ pairs are used as signal. The $\mathcal{B}$ values are chosen to be those of an SM-like Higgs boson (H_{SM}) of the corresponding mass [10], as calculated using HDECAY 6.61 [30, 31]. The $\mathcal{B}$ values decrease for larger H_1 masses as the virtual WW^* and ZZ^* decay channels, both of which have sizeable leptonic branching fractions, become more accessible. The region $m_{\text{H}_1} < m_{\text{Z}}$ is therefore where the $p_{\text{T}}^{\text{miss}}$-suppressed all-jet signature is of greatest experimental importance. Nevertheless, to preserve generality, this search attempts to probe as much of the region $m_{\text{H}_1} < 125\,\text{GeV}$ as possible.

Table 2: The m_{H_1} values in this search and corresponding $\text{H}_1 \to \text{b}\bar{\text{b}}$ branching fractions.

m_{H_1} [GeV]	30	35	40	50	60	70	80	90	100	110	120	125
$\mathcal{B}(\text{H}_1 \to \text{b}\bar{\text{b}})$	0.86	0.86	0.86	0.86	0.85	0.84	0.83	0.81	0.79	0.75	0.65	0.58

In addition to m_{H_1} and m_{SUSY}, there are two other unknown masses in the benchmark model: those of the $\tilde{\chi}_{\text{S}}^0$ and the $\tilde{\chi}_2^0$. The corresponding degrees of freedom are parameterised by $R_m \equiv m_{\text{H}_1}/m_{\tilde{\chi}_2^0}$ and $\Delta_m \equiv m_{\tilde{\chi}_2^0} - m_{\text{H}_1} - m_{\tilde{\chi}_{\text{S}}^0}$. The $p_{\text{T}}^{\text{miss}}$-suppressed signature arises for values of R_m close to unity, provided $\Delta_m > 0$ to permit the $\tilde{\chi}_2^0 \to \text{H}_1 + \tilde{\chi}_{\text{S}}^0$ decay. In this case, the phase space for the $\tilde{\chi}_2^0$ decay is small and the $\tilde{\chi}_{\text{S}}^0$ has much smaller mass than the H_1, so the $\tilde{\chi}_{\text{S}}^0$ always carries much less momentum than the H_1. The $p_{\text{T}}^{\text{miss}}$-suppressed signature probed in this search is representative of a significant part of the model parameter space since the momenta of reconstructed objects do not exhibit a strong dependence on R_m and Δ_m in the region $R_m > 0.9$. Models with smaller R_m can be probed by $p_{\text{T}}^{\text{miss}}$-based searches [10, 12]. For the benchmark model, the values $R_m = 0.99$ and $\Delta_m = 0.1\,\text{GeV}$ are assumed.

Branching fractions of unity are assumed for the decays $\tilde{\text{q}} \to \text{q} + \tilde{\chi}_2^0$ and $\tilde{\chi}_2^0 \to \text{H}_1 + \tilde{\chi}_{\text{S}}^0$. In the R_m and Δ_m region of the benchmark model, this is true except where $m_{\tilde{\chi}_2^0} > m_{\text{Z}} + m_{\tilde{\chi}_{\text{S}}^0}$. In that case, the $\tilde{\chi}_2^0 \to \text{Z} + \tilde{\chi}_{\text{S}}^0$ decay is permitted if the $\tilde{\chi}_2^0$ has a higgsino component [11]. However,

the $\widetilde{\chi}_2^0$ is expected to be mainly bino-like for relevant values of its mass [10]. For configurations where the H_1 mass is close to that of the H_{SM}, the decay $\widetilde{\chi}_2^0 \to H_{SM} + \widetilde{\chi}_S^0$ is also possible. The signatures for such H_1 and H_{SM} bosons are indistinguishable in this search. The assumption that the branching fraction for $\widetilde{\chi}_2^0 \to H_1 + \widetilde{\chi}_S^0$ decay is 100% can therefore be relaxed to the assumption that the branching fractions to H_1 and H_{SM} sum to unity.

3 The CMS detector

The central feature of the CMS apparatus is a superconducting solenoid of 6 m internal diameter, providing a magnetic field of 3.8 T. A silicon pixel and strip tracker, a lead tungstate crystal electromagnetic calorimeter, and a brass and scintillator hadron calorimeter, each composed of a barrel and two endcap sections, reside within the solenoid volume. Forward calorimeters extend the pseudorapidity (η) coverage provided by the barrel and endcap detectors. Muons are measured in gas-ionisation detectors embedded in the steel flux-return yoke outside the solenoid. Events of interest are selected using a two-tiered trigger system. The first level, composed of custom hardware processors, uses information from the calorimeters and muon detectors to select events at a rate of around 100 kHz within a fixed latency of about 4 μs [32]. The second level, known as the high-level trigger, consists of a farm of processors running a version of the full event reconstruction software optimised for fast processing, and reduces the event rate to around 1 kHz before data storage [33]. A more detailed description of the CMS detector, together with a definition of the coordinate system and the kinematic variables, can be found in Ref. [34].

4 Event simulation

The primary background in this search originates from multijet production. Simulated multijet events are used to validate the multijet background estimation based on data (described in Section 6), but are not used for any of the final predictions. The remaining significant background is from events with vector bosons that decay into quark-antiquark pairs. Simulated events are used to determine the contributions from $\mathrm{t\bar{t}}$, Z+jets, and W+jets production. The expected yields from all other SM sources of background are found to be negligible.

The multijet, Z+jets, and W+jets processes are simulated at leading order (LO) in perturbative quantum chromodynamics (QCD) using MADGRAPH5_aMC@NLO 2.4.2 [35] with up to four additional partons at the matrix element (ME) level. Simulated signal events for each pair of m_{H_1} and m_{SUSY} values of the benchmark model are generated at LO at the ME level with up to one additional parton using MADGRAPH5_aMC@NLO 2.3.3. The MLM [36] prescription is used to match partons from the LO ME calculations to those from the parton showers. Simulated $\mathrm{t\bar{t}}$ events are produced at NLO in QCD at the ME level with the POWHEG v2.0 [37–40] generator. The NNPDF2.3, NNPDF3.0, and NNPDF3.1 [41–44] parton distribution functions (PDFs) are used for the signal, 2016 background, and 2017–2018 background simulations, respectively. The parton shower and hadronisation are performed via PYTHIA 8.2 [45]. The CUETP8M1 [46, 47] tune is used for the signal and 2016 background simulations, while the CP5 tune [48] is used for the 2017 and 2018 background simulations. The cross section used to normalise the $\mathrm{t\bar{t}}$ simulation is calculated at NNLO+NNLL in QCD [49], and those for Z+jets and W+jets are calculated at NNLO in QCD [50–52]. Additional pp interactions within the same or nearby bunch crossings (pileup) are simulated for all events according to the distribution of the number of interactions observed in each bunch crossing [53]. The interactions of particles with the CMS detector are simulated using GEANT4 [54].

5 Object reconstruction and event selection

The data are collected using triggers based on the scalar sum of jet p_T (H_T), with a requirement of $H_T > 900\,\text{GeV}$ (2016) and $H_T > 1050\,\text{GeV}$ (2017 and 2018). Events are reconstructed offline using a particle-flow (PF) algorithm [55] that reconstructs and identifies each individual particle (PF candidate) in an event using an optimised combination of information from the components of the CMS detector.

Jets are reconstructed by clustering the PF candidates using the anti-k_T clustering algorithm [56], as implemented in the FASTJET package [57]. A distance parameter of 0.4 or 0.8 is used for standard- and large-radius jets, referred to as AK4 and AK8 jets, respectively. The jet momentum is defined as the vectorial sum of all particle momenta in the jet. To mitigate the effect of pileup, constituent charged PF candidates identified to be originating from vertices other than the primary pp interaction vertex are not used in the clustering algorithm. The primary vertex is taken to be the vertex corresponding to the hardest scattering in the event, evaluated using tracking information alone, as described in Section 9.4 of Ref. [58]. For AK4 jets, an offset correction is applied to correct for remaining pileup contributions. For AK8 jets, the pileup-per-particle identification algorithm [59, 60] is used to rescale the momenta of constituent neutral particles according to the probability they originated from the primary vertex. This probability is based on a local shape variable that distinguishes between collinear and soft diffuse distributions of the surrounding charged particles that are compatible with the primary vertex. For all jets, jet energy corrections are derived from simulation to bring the measured average response of jets to that of particle-level jets. In situ measurements of the momentum balance in dijet, photon+jet, Z+jet, and multijet events are used to account for any residual differences in jet energy scale and resolution between data and simulation [61, 62]. Additional criteria are imposed to reject jets from spurious sources, such as electronics noise and detector malfunctions [63, 64].

The identification of AK8 jets originating from two collimated b quarks (double-b tagging) is integral to the reconstruction of the H_1. A discriminant is calculated for each jet using a double-b tagging algorithm that combines tracking and vertexing information in a multivariate approach with no significant dependence on jet mass or p_T [65].

The event preselection requires two AK8 jets with $p_T > 170\,\text{GeV}$ and $|\eta| < 2.4$ (so that they are within the acceptance of the tracker). If there are more than two candidate AK8 jets, the two with the largest double-b tag discriminants are selected as most likely to have originated from $H_1 \to b\bar{b}$ decays. For the offline analysis, H_T is defined as the scalar p_T sum of all AK4 jets with $p_T > 40\,\text{GeV}$ and $|\eta| < 3.0$, including AK4 jets with PF candidates clustered into AK8 jets. The H_T distributions for various simulated signal and background processes are shown in Fig. 2, after implementing all preselection requirements. Since the final state contains only jets, the average signal event H_T depends significantly on m_{SUSY}, and signal events with $m_{SUSY} > 1200\,\text{GeV}$ tend to have $H_T > 1500\,\text{GeV}$.

Additional requirements based on the expected kinematic properties of signal events are applied after the preselection. They define the kinematic event selection:

1. Both selected AK8 jets must have $p_T > 300\,\text{GeV}$ and $|\eta| < 2.4$, typical of jets originating from $H_1 \to b\bar{b}$ decays.

2. There must be at least one AK4 jet with $p_T > 300\,\text{GeV}$ and $|\eta| < 3.0$, typical of quarks produced in the squark decays illustrated in Fig. 1. Such jets must be separated by $\Delta R \equiv \sqrt{(\Delta\phi)^2 + (\Delta\eta)^2} > 1.4$ from both selected AK8 jets, to avoid being constructed from the same PF candidates.

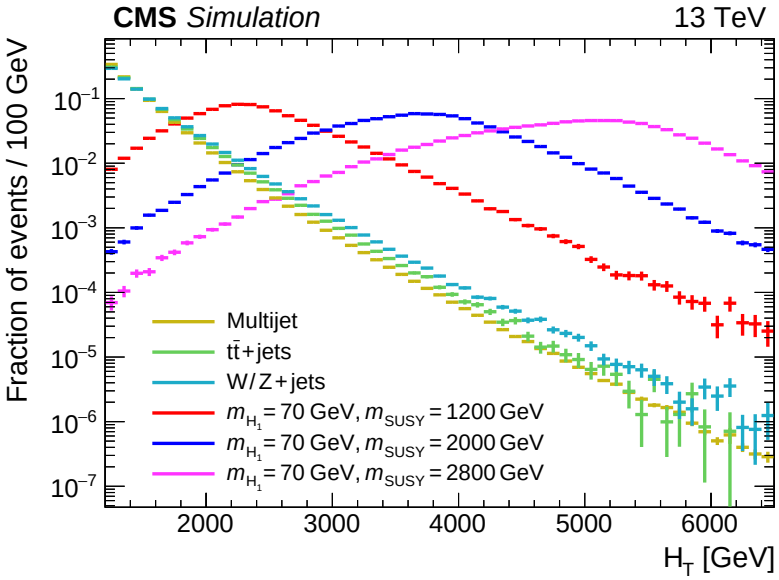

Figure 2: The H_T distribution in signal events with different values of m_{SUSY}, and in the simulated SM backgrounds, normalised to unit area. The uncertainties are statistical. All events satisfy the preselection.

3. The event H_T must exceed 1500 GeV.

Although the offline H_T resolution is better than that of the trigger-level variable, the offline H_T threshold is comfortably above the trigger-level H_T requirements. The trigger efficiency for this analysis is measured using events collected with a single muon trigger with a muon p_T threshold between 24 and 27 GeV. The efficiency for each data-taking year is nearly 100%. For the 2018 data, the $|\eta|$ selection for the AK4 jets is reduced from 3.0 to 2.4 to avoid a region of the endcap electromagnetic calorimeters affected by large losses in crystal transparency, and therefore increased energy-equivalent electronics noise [66]. This change has a negligible effect on signal acceptance for all considered masses.

The fraction of signal events that satisfy the kinematic selection is essentially independent of m_{H_1}. It increases from about 60 to 80% as m_{SUSY} increases from 1200 to 2000 GeV, after which it remains approximately constant.

5.1 Double-b tag based event selection

The two AK8 jets that are classified as the $H_1 \to b\bar{b}$ candidates in each event are randomly assigned the labels "A" and "B". Their double-b tag discriminants define a two-dimensional (2D) parameter space, as shown in Fig. 3 for simulated signal and multijet events. The signal events are expected to contain two $H_1 \to b\bar{b}$ decays and therefore accumulate in the region where both double-b tag discriminants are large. The tag region (TR) is defined as the region where the sum of the two double-b tag discriminants exceeds 1.3, illustrated by the shaded triangle in Fig. 3. Two additional regions are defined in Fig. 3: the control region (CR), a multijet-dominated region with negligible signal; and the validation region (VR), a more signal-like region where one of the two jets has a large double-b tag discriminant. The VR is defined sufficiently far from the TR for the signal contamination to be negligible.

About 50% of the signal events that satisfy the kinematic selection populate the TR, with variation at the level of $\pm 10\%$ across the m_{H_1} and m_{SUSY} parameter space considered. Since the

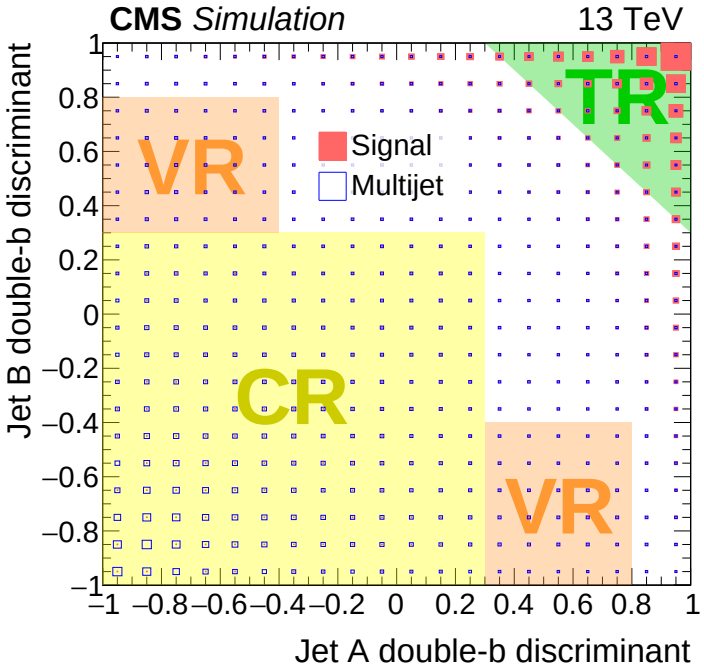

Figure 3: Distributions of simulated signal and multijet events in the 2D double-b tag discriminant plane, where the fractions of events in each bin are represented by the areas of the filled red and open blue squares, respectively. The signal parameters are $m_{\mathrm{H}_1} = 70\,\mathrm{GeV}$ and $m_{\mathrm{SUSY}} = 2000\,\mathrm{GeV}$. The kinematic selection is implemented with the masses of the two AK8 jets required to be within the set of signal and sideband mass regions defined in Section 5.2. The green, yellow, and orange shaded areas represent the tag region (TR), control region (CR), and validation region (VR), respectively. Of the plotted signal events, 65% fall within the TR.

multijet background is dominated by light-flavour quark and gluon initiated jets, only about 3% of these events populate the TR. For the $\mathrm{t\bar{t}}$, Z+jets, and W+jets backgrounds, the corresponding figures are 13, 6, and 3%, respectively.

5.2 Soft-drop mass based signal and sideband regions

In signal events, both selected AK8 jets are likely to originate from $\mathrm{H}_1 \to \mathrm{b\bar{b}}$ decays and therefore have a jet mass close to m_{H_1}. The multijet background has no resonant mass peak, while the other backgrounds are only expected to exhibit peaks near the known top quark and vector bosons masses, which means that an accurate reconstruction of the jet mass is important in distinguishing signal from background. The AK8 jet masses are evaluated using the "soft-drop" algorithm [67] (with a soft-drop threshold of $z_{\mathrm{cut}} = 0.1$ and angular exponent of $\beta = 0$), in which wide-angle soft radiation is removed recursively from a jet. In signal events this algorithm achieves a relative jet mass resolution from 10% for $m_{\mathrm{H}_1} = 125\,\mathrm{GeV}$ to 20% for $m_{\mathrm{H}_1} = 30\,\mathrm{GeV}$.

The soft-drop masses of the two AK8 jets define a 2D parameter space, shown in Fig. 4, in which 10 signal regions (S_i) and 10 sideband regions (U_i) are defined. The S_i contain events in which the two H_1-candidate jets have approximately the same soft-drop mass. The width of each S_i corresponds to about four times the experimental soft-drop mass resolution for the relevant simulated value of m_{H_1}.

The event distributions for a set of signal models with different m_{H_1} values are shown in Fig. 5,

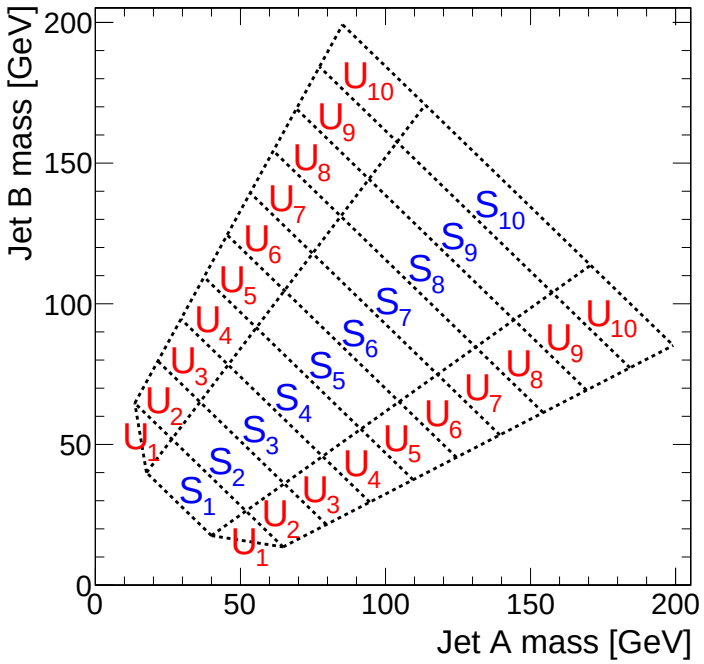

Figure 4: Map of mass regions used in the 2D soft-drop mass plane. The regions labelled S_i are the signal mass regions, and the disjoint regions U_i form the corresponding sidebands.

with the signal and sideband mass regions overlaid. The peaks in the signal distributions where one or both AK8 jets have a soft-drop mass close to zero result from a selected jet originating from a single parton or one of the $H_1 \to b\bar{b}$ decays lying outside the acceptance of the jet reconstruction algorithm. The latter can happen when the angular separation of the b quarks exceeds the AK8 jet distance parameter, or when the ratio of the b quark p_T values is larger than 9 (such that the softer b quark would not satisfy the z_{cut} threshold in the soft-drop algorithm). For signal models with $40 < m_{H_1} < 125\,\text{GeV}$, $\approx$50% of the events that satisfy the kinematic and TR selection fall within any of the S_i. However, for $m_{H_1} < 35\,\text{GeV}$ the bulk of the distribution is lower in mass than S_1, leading to a rapid decrease in signal acceptance.

The distributions of background events are also shown in Fig. 5. The majority of multijet events contain at least one AK8 jet evaluated to have a small soft-drop mass, reflecting the characteristic one-prong structure of quark and gluon jets. After applying the kinematic and TR selection criteria, approximately 5% of multijet events fall within any of the S_i, with greater probability at small masses. For the vector boson and $t\bar{t}$ backgrounds the corresponding figures are 7 and 19%, respectively, concentrated in the S_i corresponding to masses between the W boson and top quark masses.

For each S_i there are two corresponding sideband regions, U_i, used for the multijet background estimation described in Section 6. The sideband regions U_1 have a triangular form to avoid the region of very small soft-drop masses, where the density from multijet events increases sharply.

5.3 Categorisation in H_T and expected yields

The selected events are classified according to three H_T categories: 1500–2500, 2500–3500, and above 3500 GeV. Each H_T category is divided into the 10 mass signal regions S_i defined in Fig. 4, resulting in a total of 30 search regions for each data-taking year. As can be seen in Fig. 6 for TR data summed over the three data-taking years, the search region yields can be visualised

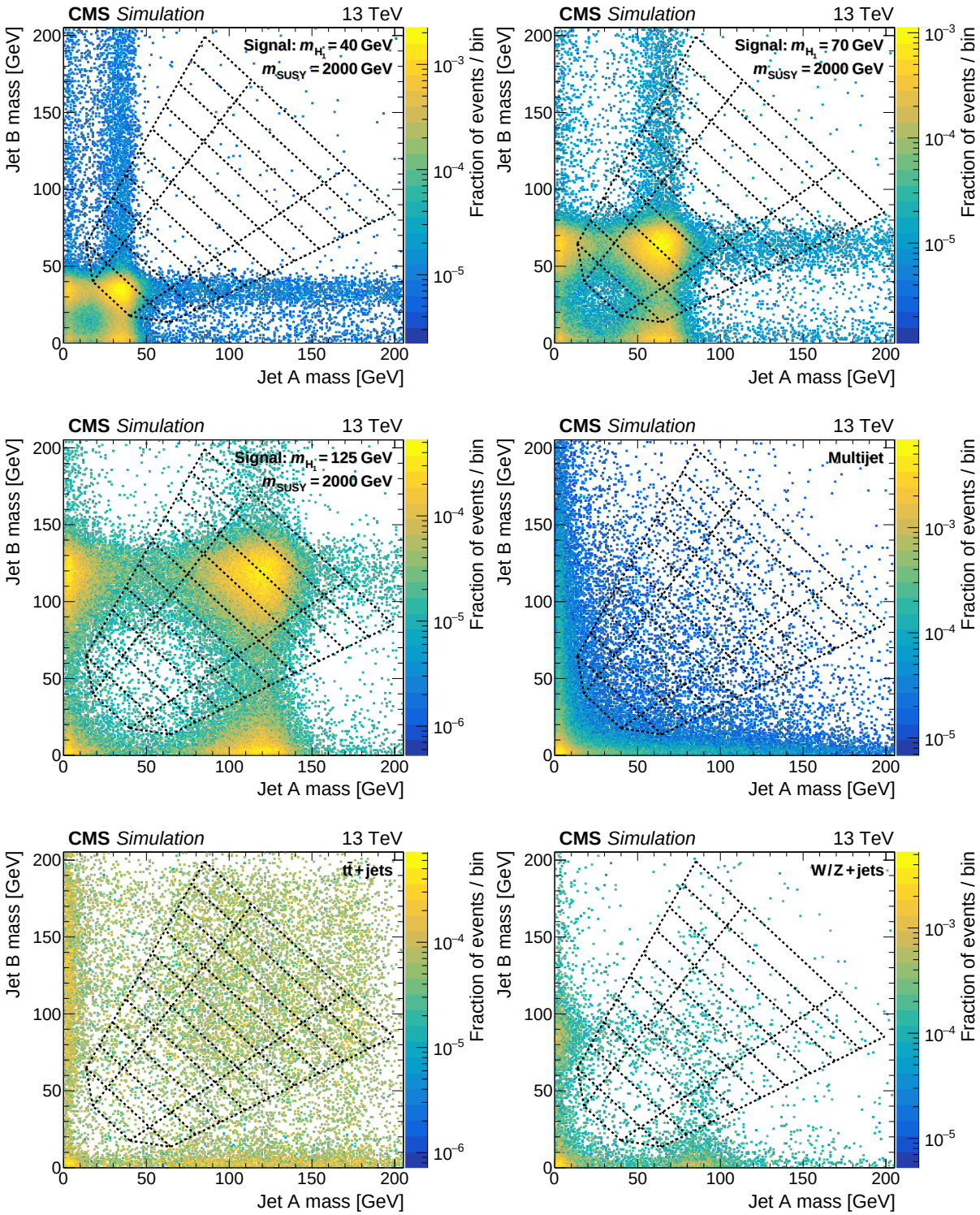

Figure 5: The normalised distribution of events in the 2D soft-drop mass plane overlaid by the map of mass regions. The upper left, upper right, and middle left panels correspond to signal events for $m_{\mathrm{SUSY}} = 2000\,\mathrm{GeV}$ and m_{H_1} values of 40, 70, and 125 GeV, respectively. The panels at middle right, lower left, and lower right correspond to simulated multijet, $\mathrm{t\bar{t}}$, and vector boson backgrounds, respectively. All events satisfy the TR requirement and the kinematic selection.

through a 30-bin histogram where bins 1–10 represent the S_i, in ascending order, for the first H_T category. The subsequent two sets of 10 bins represent the results for the second and third H_T categories. The primary background is from multijet events, estimated from data using the method described in Section 6. The expected contribution from $t\bar{t}$ events is also significant, particularly in the larger soft-drop mass regions populated by jets from hadronic top quark or W boson decays. This prediction is validated in a dedicated $t\bar{t}$-enriched control region in data. The yields from Z+jets and W+jets production are small in comparison. All expected SM backgrounds tend to exhibit small values of H_T compared to signal.

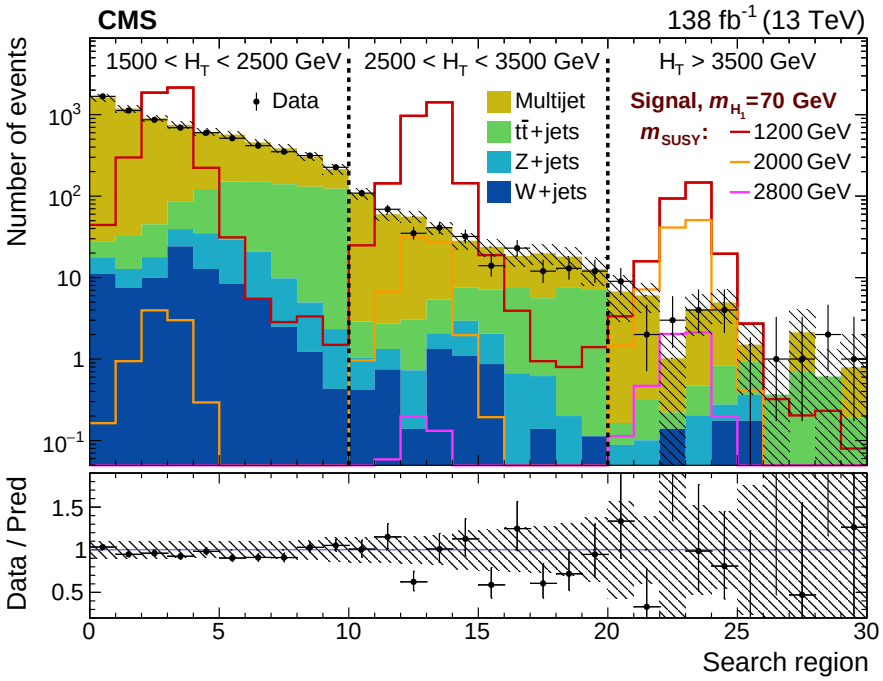

Figure 6: Observed and expected yields in the TR for each of the 30 search regions, summed over the three data-taking years. The multijet background is estimated from data using the method described in Section 6, while the other backgrounds are simulated. Example signal distributions are shown for $m_{H_1} = 70\,\text{GeV}$ and $m_{SUSY} = 1200$, 2000, and 2800 GeV. The error bars represent the statistical uncertainties and the hatched bands the systematic uncertainties.

The distributions in signal events for $m_{H_1} = 70\,\text{GeV}$ and $m_{SUSY} = 1200$, 2000 and 2800 GeV are also shown in Fig. 6. Although the production cross section decreases quickly with increasing m_{SUSY}, the fraction of events in the larger-H_T categories increases. Within each H_T category, the distribution of events in the 10 S_i bins is described by a peak with a width of about three bins, centred near the model value of m_{H_1}.

6 Multijet background estimation from data

The mass sideband regions U_i form a basis for using data to estimate the multijet background. The density of the multijet background is approximately uniform within each of the 10 mass regions (spanning S_i and U_i for each region i illustrated in Fig. 4). Apart from U_1, each U_i is constructed to have the same area as S_i such that the corresponding multijet yields, respectively denoted $\hat{U}_i$ and $\hat{S}_i$, are approximately equal. The observed ratios of S_i to U_i yields, F_i, are measured in CR data. The F_i factors are found to be close to unity except for the F_1 values which are approximately 1.5.

The multijet background in the TR is estimated independently for each signal region S_i:

$$\hat{S}_i^{\mathrm{TR}} = F_i \, \hat{U}_i^{\mathrm{TR}}, \tag{1}$$

where $\hat{U}_i^{\mathrm{TR}}$ is the observed TR yield in sideband region U_i after subtracting the contributions from the other simulated backgrounds. In rare cases where the prediction $\hat{S}_i^{\mathrm{TR}}$ is negative, it is set equal to zero.

Since the F_i factors are measured and applied in different regions of double-b tag discriminant space, any correlation between the soft-drop mass and the double-b tag discriminant of AK8 jets can bias the prediction of Eq. (1). Using a sample of data satisfying an alternative kinematic event selection with the requirement for one or more AK4 jets inverted, the variation of F_i between the TR and the CR is found to be less than 10%.

The overall accuracy of the multijet estimation is assessed through closure tests. First the method is applied to simulated multijet events in the TR where, within statistical uncertainties, the predicted yields are consistent with the simulated yields for each data-taking year. Second the method is applied in the multijet-dominated VR data (defined in Fig. 3) by making the appropriate modification to Eq. (1): $\hat{S}_i^{\mathrm{VR}} = F_i \, \hat{U}_i^{\mathrm{VR}}$. The resulting predicted and observed VR yields are consistent within uncertainties, as shown in Fig. 7. Based on the results of the closure tests, a systematic uncertainty of 15 (30%) is assigned in the lower two H_{T} categories (upper H_{T} category).

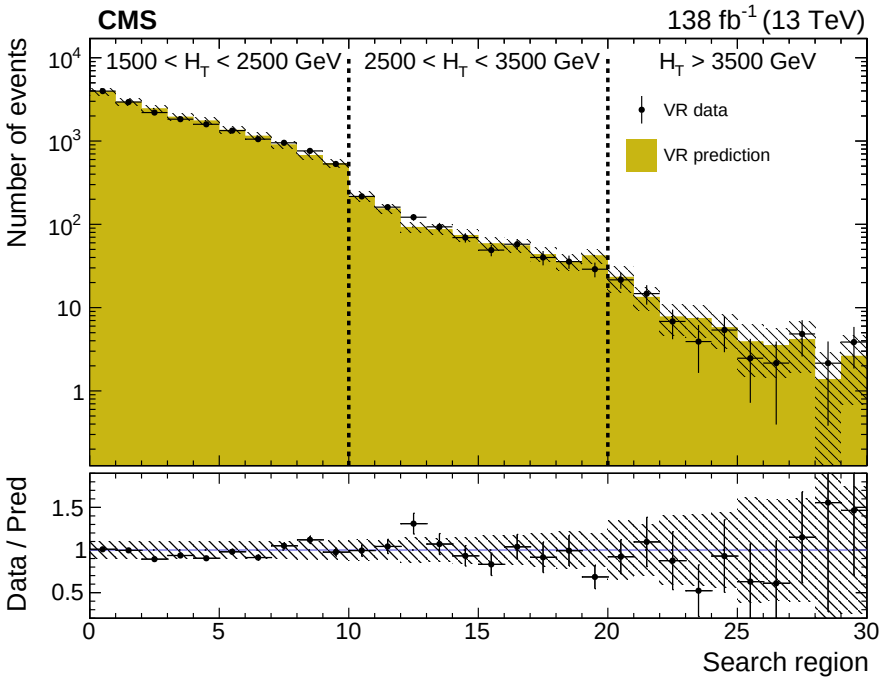

Figure 7: A comparison of the predicted and observed multijet yields in the validation region (VR), after subtraction of the other simulated backgrounds. The prediction is made separately for the three data-taking years, and the results are summed. The error bars on the data points represent their statistical uncertainties. The uncertainties in the predicted yields (statistical and systematic) are indicated by the hatched bands.

7 Systematic uncertainties

The simulated events for signal and the $\mathrm{t\bar{t}}$, Z+jets, and W+jets backgrounds are affected by various systematic uncertainties. The efficiency for tagging (mistagging) a jet originating from two b quarks (a light-flavour quark or gluon) is corrected to match that observed in data [65]. The uncertainty in this correction corresponds to $\approx 10\%$ in the simulated signal and background yields. The uncertainties related to the jet energy corrections are applied to the jet properties in bins of p_{T} and η. These uncertainties affect the event H_{T}, leading to an $\approx 4\%$ migration of events between adjacent H_{T} categories. The uncertainty in the soft-drop mass scale in simulation relative to data leads to a migration of events between adjacent S_i and U_i regions of up to 10%. The uncertainty in the simulated soft-drop mass resolution affects the widths of the simulated mass peaks. This effect is larger for signal models with small m_{H_1} and can reduce the S_i selection efficiency by up to 20%.

The systematic uncertainties are assumed to be fully correlated among the data-taking years except for the 2016 double-b tagging uncertainties, which are assumed uncorrelated because the CMS pixel detector was upgraded prior to 2017 data-taking. Changing these correlation assumptions is found to have only a small effect on the final results. Systematic uncertainties related to integrated luminosity, pileup, PDFs, renormalisation and factorisation scales, modelling of initial-state radiation, and background cross sections were also evaluated, along with the statistical uncertainties in the simulation, and were found to make negligible contributions to the total uncertainty.

Systematic uncertainties in multijet yields arise from the systematic uncertainties in the F_i factors. As described in Section 6, an uncertainty of 15% is applied to the F_i in the lower two H_{T} categories and 30% in the upper H_{T} category, uncorrelated among different F_i. Except in the lowest H_{T} category, the total uncertainty in the multijet yield is dominated by the statistical uncertainty in $\hat{U}_i^{\mathrm{TR}}$.

8 Results

Binned maximum likelihood fits to the data in all 30 search regions S_i for each data-taking year are carried out under background-only and signal+background hypotheses. The corresponding sideband regions U_i are fitted simultaneously, thereby constraining the multijet contributions to the search region yields through Eq. (1). The likelihood functions are defined through the product of 90×2 Poisson distributions [68], one for each search region and one for each sideband region, with additional constraint terms for the "nuisance" parameters that account for the systematic uncertainties summarised in Section 7. Figure 8 compares the result of the background-only fit to the yields in the search regions for the combination of 2016, 2017, and 2018 data. There is no evidence for deviations of the data from the fitted background. The values and uncertainties of most nuisance parameters are unchanged in the fit, but the ones corresponding to the F_i are constrained through Eq. (1) when the yields $\hat{S}_i^{\mathrm{TR}}$ and $\hat{U}_i^{\mathrm{TR}}$ are sufficiently large.

Signal+background fits are used to set 95% confidence level (CL) upper limits on the product $\sigma\mathcal{B}^2$ for the mass points in the benchmark signal model. The limits are set using the modified frequentist $\mathrm{CL_s}$ criterion [69, 70], with the profile likelihood ratio as test statistic [68]. The observed and expected 95% CL upper limits on $\sigma\mathcal{B}^2$ are shown in Fig. 9, as functions of m_{H_1} for constant m_{SUSY}. The upper limits are weaker for models with $m_{\mathrm{H}_1} < 35\,\mathrm{GeV}$, for which the signal-event distribution in the 2D soft-drop mass plane peaks outside the signal regions. The limits have no significant dependence on m_{SUSY} for models with $m_{\mathrm{SUSY}} > 2000\,\mathrm{GeV}$, whose

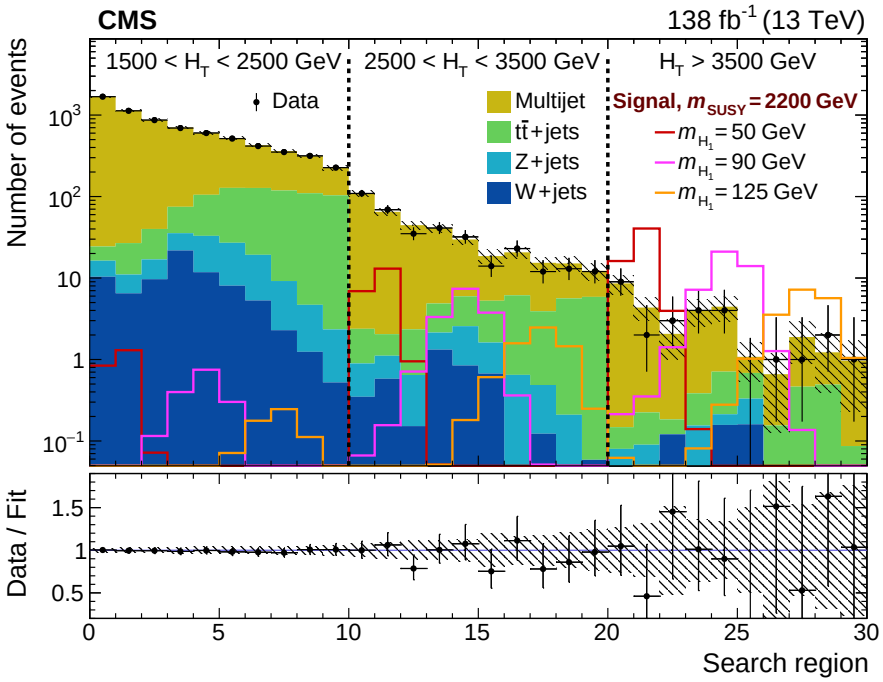

Figure 8: Yields in all search regions after the background-only fit, summed over the three data-taking years. Example signal contributions used in the signal+background fits are shown for $m_{\mathrm{SUSY}} = 2200\,\mathrm{GeV}$, and $m_{\mathrm{H}_1} = 50$, 90, and 125 GeV. The error bars represent the statistical uncertainties and the hatched bands the systematic uncertainties.

signal events mostly populate the upper H_{T} category (as shown in Fig. 6).

The $\sigma\mathcal{B}^2$ upper limits are used in conjunction with the theoretical σ and $\mathcal{B}$ values from Section 2 to exclude ranges of masses in m_{H_1} and m_{SUSY} in the benchmark model. The observed 95% CL upper limits on r, the ratio of measured and theoretical values of $\sigma\mathcal{B}^2$, are shown in Fig. 10, with the corresponding exclusion contours at $r = 1$. Masses $1200 < m_{\mathrm{SUSY}} < 2500\,\mathrm{GeV}$ are excluded within the range $40 < m_{\mathrm{H}_1} < 120\,\mathrm{GeV}$. Expected exclusion contours for the background-only scenario agree within one standard deviation with the observed contours. In the region $110 < m_{\mathrm{H}_1} < 125\,\mathrm{GeV}$, $\mathcal{B}$ starts to decrease more quickly (as shown in Table 2), leading to a corresponding reduction in sensitivity. Most of the sensitivity at large m_{SUSY} comes from the $H_{\mathrm{T}} > 3500\,\mathrm{GeV}$ region, where the statistical uncertainties in the observed yields are dominant over systematic uncertainties. This search does not explore the region outside of that shown in Fig. 10.

To aid reinterpretation of the search by reducing the model-dependence, limits evaluated using only the upper H_{T} category are presented in Appendix A. Tabulated results are provided in the HEPData record for this analysis [71].

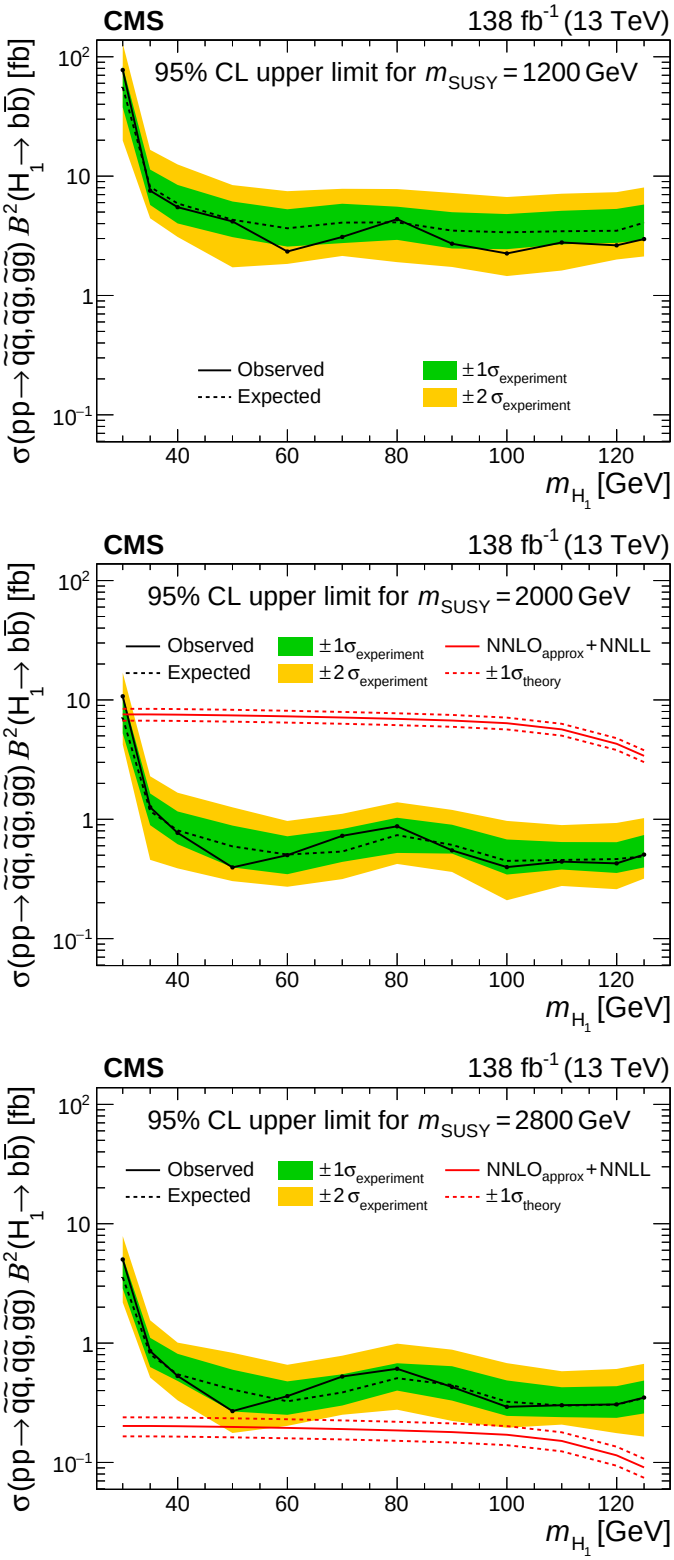

Figure 9: Upper limits at 95% CL on $\sigma\mathcal{B}^2$ as a function of m_{H_1}, for m_{SUSY} values of 1200 (upper), 2000 (middle), and 2800 GeV (lower). The solid and dashed black lines indicate the observed and median expected limits, respectively. The inner (green) band and the outer (yellow) band indicate the regions containing 68 and 95%, respectively, of the distribution of limits expected under the background-only hypothesis. The solid and dashed red lines show the theoretical value of $\sigma\mathcal{B}^2$ and its uncertainty [21–30]. In the upper plot, these $\sigma\mathcal{B}^2$ values are beyond the maximum of the vertical axis.

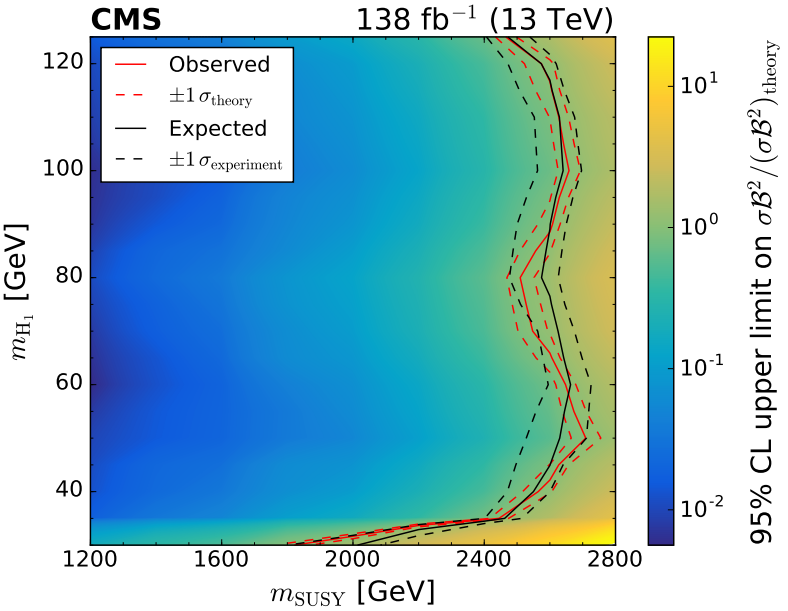

Figure 10: The observed 95% CL upper limit on $\sigma\mathcal{B}^2/(\sigma\mathcal{B}^2)_{\text{theory}}$, quantified by the colour scale as a function of m_{H_1} and m_{SUSY}. The solid and dashed red lines indicate the observed excluded region and its theoretical uncertainty, respectively. The solid and dashed black lines respectively represent the expected excluded region and its 68% CL interval, under the background-only hypothesis.

9 Summary

This paper presents a search for pairs of light Higgs bosons (H_1) produced in supersymmetric cascade decays. The targeted final states have small amounts of missing transverse momentum and two $\text{H}_1 \to \text{b}\overline{\text{b}}$ decays that are reconstructed as large-radius jets using substructure techniques. The search is based on data from pp collisions collected by the CMS experiment at $\sqrt{s} = 13\,\text{TeV}$ during 2016–2018, corresponding to an integrated luminosity of $138\,\text{fb}^{-1}$.

With no evidence found for an excess of events beyond the background expectations of the standard model (SM), the results are interpreted in the next-to-minimal supersymmetric extension of the SM (NMSSM), where a "singlino" of small mass leads to squark and gluino cascade decays that can predominantly end in a highly Lorentz-boosted singlet-like H_1 and a singlino-like neutralino of small transverse momentum.

Upper limits are set on the product of the production cross section and the square of the $\text{b}\overline{\text{b}}$ branching fraction of the H_1 for an NMSSM benchmark model with almost mass-degenerate gluinos and light-flavour squarks and branching fractions of unity for the cascade decays ending with the H_1. Under the assumption of an SM-like $\text{H}_1 \to \text{b}\overline{\text{b}}$ branching fraction, H_1 bosons with masses in the range 40–120 GeV, arising from the decays of squarks or gluinos with a mass from 1200 to 2500 GeV, are excluded at 95% confidence level.

References

[1] P. Ramond, "Dual theory for free fermions", *Phys. Rev. D* **3** (1971) 2415, doi:10.1103/PhysRevD.3.2415.

[2] Y. A. Golfand and E. P. Likhtman, "Extension of the algebra of Poincaré group generators and violation of P invariance", *JETP Lett.* **13** (1971) 323.

[3] A. Neveu and J. H. Schwarz, "Factorizable dual model of pions", *Nucl. Phys. B* **31** (1971) 86, doi:10.1016/0550-3213(71)90448-2.

[4] D. V. Volkov and V. P. Akulov, "Possible universal neutrino interaction", *JETP Lett.* **16** (1972) 438.

[5] J. Wess and B. Zumino, "A Lagrangian model invariant under supergauge transformations", *Phys. Lett. B* **49** (1974) 52, doi:10.1016/0370-2693(74)90578-4.

[6] J. Wess and B. Zumino, "Supergauge transformations in four dimensions", *Nucl. Phys. B* **70** (1974) 39, doi:10.1016/0550-3213(74)90355-1.

[7] P. Fayet, "Supergauge invariant extension of the Higgs mechanism and a model for the electron and its neutrino", *Nucl. Phys. B* **90** (1975) 104, doi:10.1016/0550-3213(75)90636-7.

[8] H. P. Nilles, "Supersymmetry, supergravity and particle physics", *Phys. Rep.* **110** (1984) 1, doi:10.1016/0370-1573(84)90008-5.

[9] U. Ellwanger, C. Hugonie, and A. M. Teixeira, "The Next-to-Minimal Supersymmetric Standard Model", *Phys. Repts.* **496** (2010) 1, doi:10.1016/j.physrep.2010.07.001, arXiv:0910.1785.

[10] U. Ellwanger and A. Teixeira, "NMSSM with a singlino LSP: possible challenges for searches for supersymmetry at the LHC", *JHEP* **10** (2014) 113, doi:10.1007/JHEP10(2014)113, arXiv:1406.7221.

[11] U. Ellwanger and A. Teixeira, "Excessive Higgs pair production with little MET from squarks and gluinos in the NMSSM", *JHEP* **04** (2015) 172, doi:10.1007/JHEP04(2015)172, arXiv:1412.6394.

[12] A. Titterton et al., "Exploring sensitivity to NMSSM signatures with low missing transverse energy at the LHC", *JHEP* **10** (2018) 064, doi:10.1007/JHEP10(2018)064, arXiv:1807.10672.

[13] CMS Collaboration, "Search for physics beyond the standard model in events with high-momentum Higgs bosons and missing transverse momentum in proton-proton collisions at 13 TeV", *Phys. Rev. Lett.* **120** (2018) 241801, doi:10.1103/PhysRevLett.120.241801, arXiv:1712.08501.

[14] CMS Collaboration, "Search for higgsinos in channels with two Higgs bosons and missing transverse momentum in proton-proton collisions at $\sqrt{s} = 13$ TeV", 2021. arXiv:2201.04206. Submitted to *JHEP*.

[15] ATLAS Collaboration, "Search for pair production of higgsinos in final states with at least three b-tagged jets in $\sqrt{s} = 13$ TeV pp collisions using the ATLAS detector", *Phys. Rev. D* **98** (2018) 092002, doi:10.1103/PhysRevD.98.092002, arXiv:1806.04030.

[16] CMS Collaboration, "Searches for electroweak neutralino and chargino production in channels with Higgs, Z, and W bosons in pp collisions at 8 TeV", *Phys. Rev. D* **90** (2014) 092007, doi:10.1103/PhysRevD.90.092007, arXiv:1409.3168.

[17] CMS Collaboration, "Search for higgsino pair production in pp collisions at $\sqrt{s}$ = 13 TeV in final states with large missing transverse momentum and two Higgs bosons decaying via $H \to b\bar{b}$", *Phys. Rev. D* **97** (2018) 032007, doi:10.1103/PhysRevD.97.032007, arXiv:1709.04896.

[18] CMS Collaboration, "Precision luminosity measurement in proton-proton collisions at $\sqrt{s} = 13$ TeV in 2015 and 2016 at CMS", *Eur. Phys. J. C* **81** (2021) 800, doi:10.1140/epjc/s10052-021-09538-2, arXiv:2104.01927.

[19] CMS Collaboration, "CMS luminosity measurement for the 2017 data-taking period at $\sqrt{s} = 13$ TeV", CMS Physics Analysis Summary CMS-PAS-LUM-17-004, 2018.

[20] CMS Collaboration, "CMS luminosity measurement for the 2018 data-taking period at $\sqrt{s} = 13$ TeV", CMS Physics Analysis Summary CMS-PAS-LUM-18-002, 2019.

[21] W. Beenakker, R. Höpker, M. Spira, and P. M. Zerwas, "Squark and gluino production at hadron colliders", *Nucl. Phys. B* **492** (1997) 51, doi:10.1016/S0550-3213(97)00084-9, arXiv:hep-ph/9610490.

[22] A. Kulesza and L. Motyka, "Threshold resummation for squark-antisquark and gluino-pair production at the LHC", *Phys. Rev. Lett.* **102** (2009) 111802, doi:10.1103/PhysRevLett.102.111802, arXiv:0807.2405.

[23] A. Kulesza and L. Motyka, "Soft gluon resummation for the production of gluino-gluino and squark-antisquark pairs at the LHC", *Phys. Rev. D* **80** (2009) 095004, doi:10.1103/PhysRevD.80.095004, arXiv:0905.4749.

[24] W. Beenakker et al., "Soft-gluon resummation for squark and gluino hadroproduction", *JHEP* **12** (2009) 041, doi:10.1088/1126-6708/2009/12/041, arXiv:0909.4418.

[25] W. Beenakker et al., "Squark and gluino hadroproduction", *Int. J. Mod. Phys. A* **26** (2011) 2637, doi:10.1142/S0217751X11053560, arXiv:1105.1110.

[26] W. Beenakker et al., "NNLL resummation for squark-antisquark pair production at the LHC", *JHEP* **01** (2012) 076, doi:10.1007/JHEP01(2012)076, arXiv:1110.2446.

[27] W. Beenakker et al., "Towards NNLL resummation: hard matching coefficients for squark and gluino hadroproduction", *JHEP* **10** (2013) 120, doi:10.1007/JHEP10(2013)120, arXiv:1304.6354.

[28] W. Beenakker et al., "NNLL resummation for squark and gluino production at the LHC", *JHEP* **12** (2014) 023, doi:10.1007/JHEP12(2014)023, arXiv:1404.3134.

[29] W. Beenakker et al., "NNLL-fast: predictions for coloured supersymmetric particle production at the LHC with threshold and Coulomb resummation", *JHEP* **12** (2016) 133, doi:10.1007/JHEP12(2016)133, arXiv:1607.07741.

[30] A. Djouadi, J. Kalinowski, and M. Spira, "HDECAY: a program for Higgs boson decays in the standard model and its supersymmetric extension", *Comput. Phys. Commun.* **108** (1998) 56, doi:10.1016/S0010-4655(97)00123-9, arXiv:hep-ph/9704448.

[31] A. Djouadi, J. Kalinowski, M. Mühlleitner, and M. Spira, "HDECAY: Twenty++ years after", *Comput. Phys. Commun.* **238** (2019) 214, doi:10.1016/j.cpc.2018.12.010, arXiv:1801.09506.

[32] CMS Collaboration, "Performance of the CMS Level-1 trigger in proton-proton collisions at $\sqrt{s} = 13\,\text{TeV}$", *JINST* **15** (2020) P10017, doi:10.1088/1748-0221/15/10/P10017, arXiv:2006.10165.

[33] CMS Collaboration, "The CMS trigger system", *JINST* **12** (2017) P01020, doi:10.1088/1748-0221/12/01/P01020, arXiv:1609.02366.

[34] CMS Collaboration, "The CMS experiment at the CERN LHC", *JINST* **3** (2008) S08004, doi:10.1088/1748-0221/3/08/S08004.

[35] J. Alwall et al., "The automated computation of tree-level and next-to-leading order differential cross sections, and their matching to parton shower simulations", *JHEP* **07** (2014) 079, doi:10.1007/JHEP07(2014)079, arXiv:1405.0301.

[36] J. Alwall et al., "Comparative study of various algorithms for the merging of parton showers and matrix elements in hadronic collisions", *Eur. Phys. J. C* **53** (2008) 473, doi:10.1140/epjc/s10052-007-0490-5, arXiv:0706.2569.

[37] S. Frixione, P. Nason, and G. Ridolfi, "A positive-weight next-to-leading-order Monte Carlo for heavy flavour hadroproduction", *JHEP* **09** (2007) 126, doi:10.1088/1126-6708/2007/09/126, arXiv:0707.3088.

[38] P. Nason, "A new method for combining NLO QCD with shower Monte Carlo algorithms", *JHEP* **11** (2004) 040, doi:10.1088/1126-6708/2004/11/040, arXiv:hep-ph/0409146.

[39] S. Frixione, P. Nason, and C. Oleari, "Matching NLO QCD computations with parton shower simulations: the POWHEG method", *JHEP* **11** (2007) 070, doi:10.1088/1126-6708/2007/11/070, arXiv:0709.2092.

[40] S. Alioli, P. Nason, C. Oleari, and E. Re, "A general framework for implementing NLO calculations in shower Monte Carlo programs: the POWHEG BOX", *JHEP* **06** (2010) 043, doi:10.1007/JHEP06(2010)043, arXiv:1002.2581.

[41] NNPDF Collaboration, "Unbiased global determination of parton distributions and their uncertainties at NNLO and LO", *Nucl. Phys. B* **855** (2012) 153, doi:10.1016/j.nuclphysb.2011.09.024, arXiv:1107.2652.

[42] NNPDF Collaboration, "Parton distributions for the LHC Run II", *JHEP* **04** (2015) 040, doi:10.1007/JHEP04(2015)040, arXiv:1410.8849.

[43] NNPDF Collaboration, "Parton distributions with QED corrections", *Nucl. Phys. B* **877** (2013) 290, doi:10.1016/j.nuclphysb.2013.10.010, arXiv:1308.0598.

[44] NNPDF Collaboration, "Parton distributions from high-precision collider data", *Eur. Phys. J. C* **77** (2017) 663, doi:10.1140/epjc/s10052-017-5199-5, arXiv:1706.00428.

[45] T. Sjöstrand et al., "An introduction to PYTHIA 8.2", *Comput. Phys. Commun.* **191** (2015) 159, doi:10.1016/j.cpc.2015.01.024, arXiv:1410.3012.

[46] CMS Collaboration, "Event generator tunes obtained from underlying event and multiparton scattering measurements", *Eur. Phys. J. C* **76** (2016) 155, doi:10.1140/epjc/s10052-016-3988-x, arXiv:1512.00815.

[47] P. Skands, S. Carrazza, and J. Rojo, "Tuning PYTHIA 8.1: the Monash 2013 tune", *Eur. Phys. J. C* **74** (2014) 3024, doi:10.1140/epjc/s10052-014-3024-y, arXiv:1404.5630.

[48] CMS Collaboration, "Extraction and validation of a new set of CMS PYTHIA8 tunes from underlying-event measurements", *Eur. Phys. J. C* **80** (2020) 4, doi:10.1140/epjc/s10052-019-7499-4, arXiv:1903.12179.

[49] M. Czakon and A. Mitov, "TOP++: a program for the calculation of the top-pair cross-section at hadron colliders", *Comput. Phys. Commun.* **185** (2014) 2930, doi:10.1016/j.cpc.2014.06.021, arXiv:1112.5675.

[50] R. Gavin, Y. Li, F. Petriello, and S. Quackenbush, "FEWZ 2.0: A code for hadronic Z production at next-to-next-to-leading order", *Comput. Phys. Commun.* **182** (2011) 2388, doi:10.1016/j.cpc.2011.06.008, arXiv:1011.3540.

[51] R. Gavin, Y. Li, F. Petriello, and S. Quackenbush, "W physics at the LHC with FEWZ 2.1", *Comput. Phys. Commun.* **184** (2013) 208, doi:10.1016/j.cpc.2012.09.005, arXiv:1201.5896.

[52] Y. Li and F. Petriello, "Combining QCD and electroweak corrections to dilepton production in FEWZ", *Phys. Rev. D* **86** (2012) 094034, doi:10.1103/PhysRevD.86.094034, arXiv:1208.5967.

[53] CMS Collaboration, "Measurement of the inelastic proton-proton cross section at $\sqrt{s} = 13$ TeV", *JHEP* **07** (2018) 161, doi:10.1007/JHEP07(2018)161, arXiv:1802.02613.

[54] GEANT4 Collaboration, "GEANT4—a simulation toolkit", *Nucl. Instrum. Meth. A* **506** (2003) 250, doi:10.1016/S0168-9002(03)01368-8.

[55] CMS Collaboration, "Particle-flow reconstruction and global event description with the CMS detector", *JINST* **12** (2017) P10003, doi:10.1088/1748-0221/12/10/P10003, arXiv:1706.04965.

[56] M. Cacciari, G. P. Salam, and G. Soyez, "The anti-k_{T} jet clustering algorithm", *JHEP* **04** (2008) 063, doi:10.1088/1126-6708/2008/04/063, arXiv:0802.1189.

[57] M. Cacciari, G. P. Salam, and G. Soyez, "FastJet user manual", *Eur. Phys. J. C* **72** (2012) 1896, doi:10.1140/epjc/s10052-012-1896-2, arXiv:1111.6097.

[58] CMS Collaboration, "Technical proposal for the Phase-II upgrade of the Compact Muon Solenoid", CMS Technical Proposal CERN-LHCC-2015-010, CMS-TDR-15-02, 2015.

[59] CMS Collaboration, "Pileup mitigation at CMS in 13 TeV data", *JINST* **15** (2020) P09018, doi:10.1088/1748-0221/15/09/p09018, arXiv:2003.00503.

[60] D. Bertolini, P. Harris, M. Low, and N. Tran, "Pileup Per Particle Identification", *JHEP* **10** (2014) 059, doi:10.1007/JHEP10(2014)059, arXiv:1407.6013.

[61] CMS Collaboration, "Jet energy scale and resolution in the CMS experiment in pp collisions at 8 TeV", *JINST* **12** (2017) P02014, doi:10.1088/1748-0221/12/02/P02014, arXiv:1607.03663.

[62] CMS Collaboration, "Jet energy scale and resolution performance with 13 TeV data collected by CMS in 2016", Detector Performance Report CMS-DP-2018-028, 2018.

[63] CMS Collaboration, "Jet performance in pp collisions at $\sqrt{s} = 7$ TeV", CMS Physics Analysis Summary CMS-PAS-JME-10-003, 2010.

[64] CMS Collaboration, "Jet algorithms performance in 13 TeV data", CMS Physics Analysis Summary CMS-PAS-JME-16-003, 2017.

[65] CMS Collaboration, "Identification of heavy-flavour jets with the CMS detector in pp collisions at 13 TeV", *JINST* **13** (2018) P05011, doi:10.1088/1748-0221/13/05/P05011, arXiv:1712.07158.

[66] T. Adams et al., "Beam test evaluation of electromagnetic calorimeter modules made from proton-damaged $PbWO_4$ crystals", *JINST* **11** (2016) P04012, doi:10.1088/1748-0221/11/04/P04012.

[67] A. J. Larkoski, S. Marzani, G. Soyez, and J. Thaler, "Soft Drop", *JHEP* **05** (2014) 146, doi:10.1007/JHEP05(2014)146, arXiv:1402.2657.

[68] ATLAS and CMS Collaborations, "Procedure for the LHC Higgs boson search combination in summer 2011", ATLAS/CMS joint note ATL-PHYS-PUB-2011-011, CMS-NOTE-2011-005, 2011.

[69] T. Junk, "Confidence level computation for combining searches with small statistics", *Nucl. Instrum. Meth. A* **434** (1999) 435, doi:10.1016/S0168-9002(99)00498-2, arXiv:hep-ex/9902006.

[70] A. L. Read, "Presentation of search results: The CL_s technique", *J. Phys. G* **28** (2002) 2693, doi:10.1088/0954-3899/28/10/313.

[71] "HEPData record for this analysis", 2022. doi:10.17182/hepdata.114359.

A Simplified analysis for reinterpretation

To aid reinterpretation of the search, a simplified analysis is performed using only the 10 search regions in the upper H_T category. The value A_{kin} is defined as the product of acceptance and efficiency for a signal event to satisfy the kinematic selection (defined in Section 5) and the $H_T > 3500\,\text{GeV}$ requirement. The value of A_{kin} is common among all 10 search regions in the simplified analysis, and is quoted for the benchmark signal model in Table A.1. Upper limits on the product $\sigma\,\mathcal{B}^2\,A_{kin}$ as a function of m_{H_1} are set in Fig. A.1, from which $\sigma\mathcal{B}^2$ limits for different signal models can be derived through division by the appropriate value of A_{kin}. Since the upper H_T category provides most of the sensitivity for $m_{SUSY} > 2000\,\text{GeV}$ in the nominal analysis, the $\sigma\mathcal{B}^2$ upper limits in this region are not much weaker in the simplified analysis. This is not the case in the region $m_{SUSY} < 2000\,\text{GeV}$, where the lower H_T categories become important.

Table A.1: Reference values of the product of kinematic acceptance and efficiency (A_{kin}) for the $H_T > 3500\,\text{GeV}$ region for the benchmark signal model with different values of m_{SUSY}. These values are independent of m_{H_1} within 2% in the range $30 < m_{H_1} < 125\,\text{GeV}$.

m_{SUSY} [GeV]	1600	2000	2200	2400	2600	2800
A_{kin}	0.17	0.46	0.58	0.66	0.71	0.74

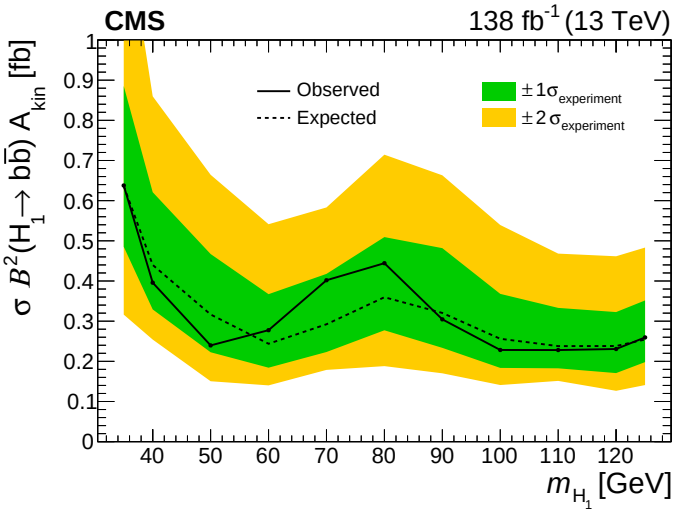

Figure A.1: The observed and expected 95% CL upper limit on the product of $\sigma\mathcal{B}^2$ and A_{kin}, the kinematic acceptance and efficiency for the $H_T > 3500\,\text{GeV}$ region, as a function of m_{H_1}. The results are independent of m_{SUSY} within 10% in the range $1600 < m_{SUSY} < 2800\,\text{GeV}$. The solid and dashed black lines indicate the observed and median expected limits, respectively. The inner (green) band and the outer (yellow) band indicate the regions containing 68 and 95%, respectively, of the distribution of limits expected under the background-only hypothesis.

The double-b tag and mass region selections are not considered in A_{kin}. This is done for simplicity, and because the fraction of events satisfying these selections is not found to be strongly model-dependent (except for the dependence on m_{H_1}, which is accounted for explicitly in Fig. A.1). For the benchmark model, this fraction is found to be independent of m_{SUSY} within 10% in the region $1600 < m_{SUSY} < 2800\,\text{GeV}$ and $35 < m_{H_1} < 125\,\text{GeV}$. This approximate independence does not hold for models with $m_{SUSY} < 1600\,\text{GeV}$, where the H_1 p_T distribution has substantial contributions below the p_T necessary for the $H_1 \to b\bar{b}$ decay products to be merged in a single AK8 jet. Only models with typical $b\bar{b}$ angular separation $\Delta R < 0.8$ should be considered for reinterpretation.